Numerical Methods in Civil Engineering

Journal Homepage: https://nmce.kntu.ac.ir/

Determining the moment-rotation curve for top and seat angle and stiffened welded-seat connections using Chisala's model

Nader Fanaie*, Mehdi Fazli **, and Mohammad Amin Moghaddasi***

ARTICLE INFO

RESEARCH PAPER

Article history:
Received:
March 2023
Revised:
June 2023
Accepted:
July 2023

Keywords:
Chisala's model, moment-rotation curve,
Top and seat angle connection,
Stiffened welded-seat connection,
Finite element analysis

Abstract:

This research aims to investigate the analytical procedure of constructing the moment-rotation curve for top and seat angle, and stiffened welded-seat connections using Chisala's model. As these connections practically exhibit a semi-rigid flexural performance, the moment-rotation curve appears to provide useful information and helpful vision on their performance for design engineers. Since the process of determining the precise moment-rotation curve for a steel connection is costly due to the need for laboratory experiments or heavy finite element computations, using a precise and straightforward analytical model appears to be more feasible. Chisala's model, having fewer and independent parameters, is precise and easy to construct, which is fit for the purpose. In this regard, the procedure of constructing the analytical model for both types of connections using Chisala's model is explained, and the key parameters of Chisala's model are determined. As a means of verification, finite element models of both types of connections were constructed as well, using Abaqus software. To ensure that the results are not accidental, a total of 34 TSA (Top and Seat Angle), and 33 SWS (Stiffened Welded-Seat) connection specimens with different geometric dimensions were tested, and the effects of geometric dimensions on the flexural performance of each type as side results were described. Based on the obtained data, analytical and numerical moment-rotation curves, for both types of connections, were illustrated. The results suggest that Chisala's model can precisely predict the moment-rotation curve for the mentioned types of connections, provided that a proper equivalent analytical model is created

1. Introduction

Generally, the performance of a structural element relies heavily upon its stiffness, strength, and ductility. The mentioned properties are important in structural design procedures. In this regard, the moment-rotation curve for a structural element is an important design tool since it indicates all of the mentioned properties as a whole. This claim is well depicted in Figure 1.

The process of determining the moment-rotation curve for a connection, or a structural element, is costly since the precise curve is derived from experiment results or several finite element analysis (FEA) procedures, therefore, using analytical models to determine the moment-rotation curve for steel connections, appears to be the most feasible approach. There are numerous analytical models introduced by researchers, each having its advantages and downsides. Most of these analytical models are described in further sections.

1.1. Power models

The most famous power model was proposed by Richard et al. in 1988 and was used to construct the moment-rotation curve for bolted double framing angle connections [1]. They collected data from laboratory tests and made an analytical model consisting of springs and rigid bars, each representing the stiffness of different components of a bolted double

** Associate Professor, Civil Engineering Department, K. N. Toosi University of Technology, Tehran, Iran. Email: fanaie@kntu.ac.ir*
*** MSc, Fakoor Sanat Tehran Engineering Company, Tehran, Iran.*
**** MSc, Civil Engineering Department, K. N. Toosi University of Technology, Tehran, Iran.*

http://doi.org/10.52547/NMCE.2303.1014

framing angle connection [1]. This spring system is shown in Figure 2.

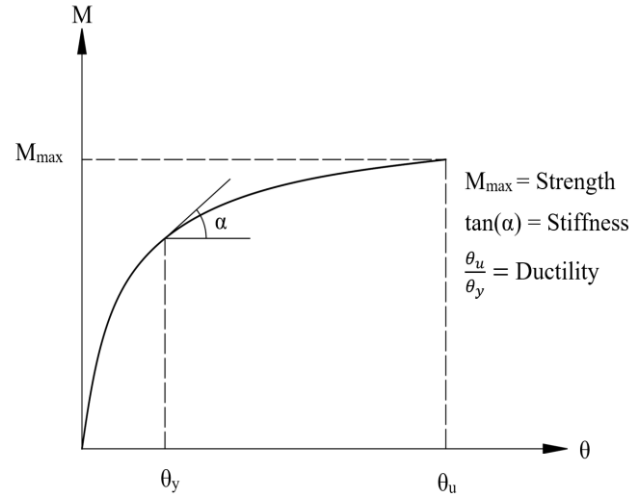

Fig. 1. The moment-rotation curve for a structural element, and its strength, stiffness, and ductility.

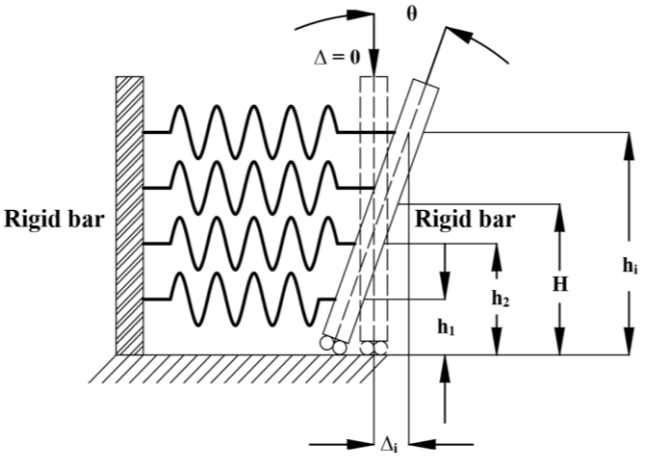

Fig. 2: Analytical model for double framing angles [1].

Using the experimental results, along with the proposed equivalent spring system, Richard et al. proposed a four-parameter power model capable of predicting the moment-rotation curve for the specified type of steel connection [1]. To verify their study, they compared the results obtained by Lewitt et al. [2] and the polynomial model proposed by Frye and Morris [3]. This comparison suggests that the proposed power model can precisely predict the moment-rotation curve for rotations larger than 0.003 radians [1]. There were other endeavors towards reaching a power model by researchers. In 1991, Attiogbe and Morris derived the parameters of Richard-Abbott [4], and Ramberg-Osgood [5] power models using selected points, and the least-squares method as curve fitting procedures [6]. They compared the results obtained from both power models and concluded that the Richard-Abbott model is relatively more precise [6]. Kishi et al. plotted the moment-rotation curve for end-plate connections using the Richard-Abbott model and verified the results with laboratory tests carried out on a total of 168 end-plate connection specimens [7]. Along with this they also proposed another power model which can be used to determine the moment-rotation curve for end-plate connections [7]. Another study aiming to verify the precision of the Richard-Abbott power model was done by Abolmaali et al. in 2005 [8]. In a recent 2020 study, Tran used the four-parameter power model proposed by Kishi et al. and extended it to determine the moment-rotation curve for semi-rigid cruciform flush end-plate connections exposed to elevated temperatures [9].

1.2. Logarithmic models

Lee and Moon proposed a two-parameter logarithmic moment-rotation model for double web angle and top and seat angle connections [10]. One of the main advantages of this model over the others is that it has fewer parameters that can be determined easily [10]. On downsides, these two parameters have no physical interpretation however, that does not affect the calculation results [10]. In 2017, Kong and Kim proposed an inverse hyperbolic moment-rotation curve for top and seat angle connections with double web angles, using the experimental data from studies done by various researchers such as Azizinamini [11], and Calado et al. [12] as verification [13]. They compared the analytical, and experimental results [13]. This comparison suggests that the proposed inverse hyperbolic model has acceptable precision in predicting the moment-rotation curve for the mentioned type of steel connection [13].

1.3. Exponential models

In 1999, Chisala proposed the following three-parameter exponential moment-rotation model for double web angle, and top and seat angle with and without double web angle connections and used the experimental results from various studies such as Azizinamini and Radziminski's work [14] on semi-rigid steel connections [15]:

$$M = \left[M_\circ + K_p\theta\right]\left[1 - exp(-K_i\theta/M_\circ)\right] \quad (1)$$

where:

M_o = The intercept-constant

K_i = The initial (elastic) stiffness of the connection

K_p = The strain-hardening (plastic) stiffness of the connection

The initial stiffness (K_i) is the slope of the moment-rotation curve at zero [15]. The plastic stiffness (K_p) is the slope of the very curve at the end of the plastic zone (before flexural failure of the connection) [15]. The intercept-constant (M_o) is a parameter responsible for controlling the overall strength of the connection [15]. These three parameters are mathematically independent and very easy to determine which makes Chisala's model relatively efficient to use.

Other exponential moment-rotation models were introduced later including Gilio et al. proposing a model for cold-formed steel purlins with sleeved bolted connection [16], Zhou et al. introducing a two-parameter exponential model for calculating the initial stiffness of beam to concrete-filled steel tube (CFT) column connections with bidirectional bolts [17], and a four-parameter exponential model proposed by Zhao et al. to predict the moment-rotation curve for eccentric rectangular hollow section (EHRS) cross-type connections subjected to out-of-plane bending moment and chor stress [18].

2. Materials and FEA reliability

To ensure that FEA results are reliable, two important matters should be considered. First, the selected material properties must be as close to actual as possible, and second, the results of the numerical modeling procedure must be in an agreement with experimental results to an acceptable degree. Considering the material properties, Mofid et al. showed that a normalized stress-strain curve can describe the performance of ordinary constructional steel to an acceptable degree [19]. Details and specifications of normalized material properties are presented in Table 1.

Table 1: Details of the normalized stress-strain curve for different steel types [19].

Steel type	σ_y MPa	σ_u MPa	ε_y	ε_p	ε_h	ε_u	E MPa	E_h MPa	E_u MPa
S235	235	360	0.0011	0.0140	0.0370	0.1400	210000	5500	360
S275	275	430	0.0013	0.0150	0.0470	0.1200	210000	4800	430
S355	355	510	0.0017	0.0170	0.0530	0.1100	210000	4250	510
Constructional steel	σ_y	1.5 σ_y	ε_y	11 ε_y	21 ε_y	121 ε_y	E	E/20	E/500

According to the data available in Table 1, S235 was selected as the main steel and S355 as weld steel. Using the data, the stress-strain curve for main and weld steel were illustrated, which are shown in Figure 3.

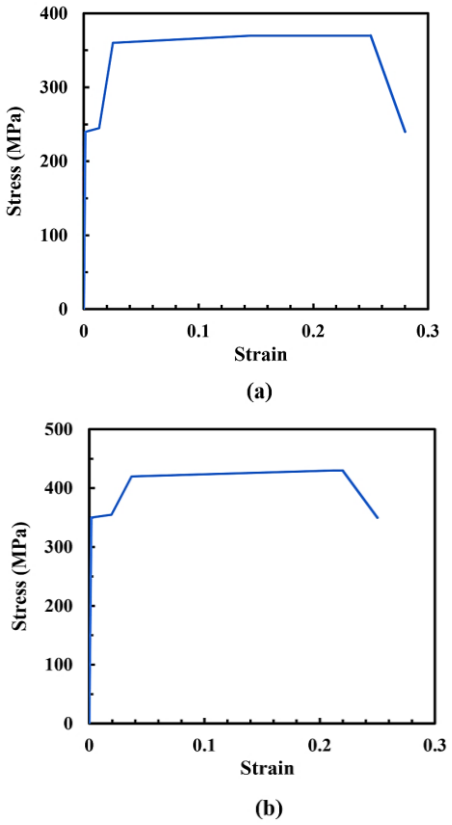

Fig. 3: Normalized stress-strain curve for (a) main steel (b) weld steel.

As for the numerical modeling procedure, finite element models were created and analyzed. The created models were the same laboratory specimens tested by Ghobadi et al. in 2009 [20]. They carried out experiments on 5 series of moment-resisting connection specimens under cyclic loading [20]. From these 5 series of specimens, 2 series were selected for modeling. These two series are RC2 (retrofitted connection) and RC4 [20]. Details of these types of connections are presented in Figure 4.

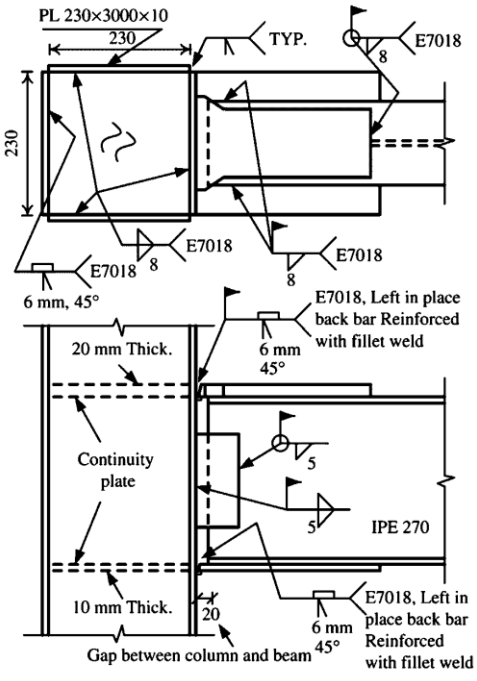

Fig. 4: Details of RC2 specimen [20].

The RC4 and RC2 are similar in detail, except for the bottom plate welds, where RC2 has a full penetration groove weld, and RC4 has a double-sided fillet weld [20]. For laboratory tests, a T-shaped full-scale test setup was employed [20], details of which are illustrated in Figure 5.

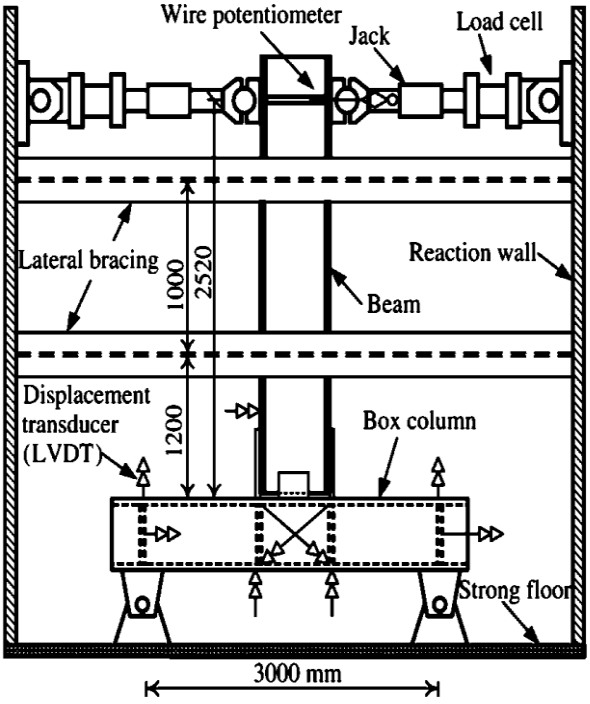

Fig. 5: Full-scale test setup [20].

These test specimens were subjected to standard cyclic loading according to FEMA [20, 21]. Finite element models were created using C3D15 and C3D20 elements (with varying dimensions and hourglass control) for main steel, and welds, respectively. The finite element model of the RC4 specimen is shown in Figure 6.

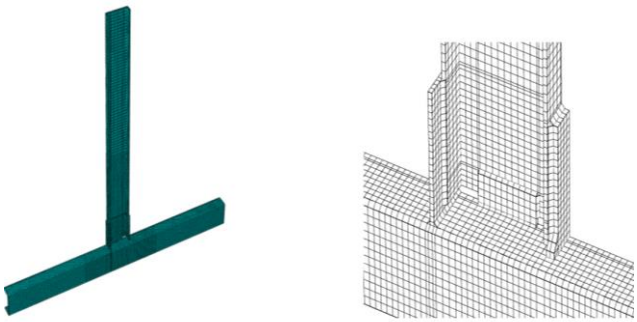

Fig. 6: Finite element model of RC4 specimen.

The numerical and experimental moment-drift angle curves for both types (RC2 and RC4) are presented in Figure 7, and Figure 8. The moment axis on these curves is normalized (M/M_p).

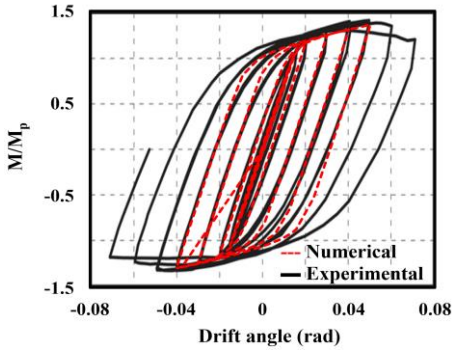

Fig. 7: Experimental [20] and numerical moment-drift angle curve for RC2 specimen.

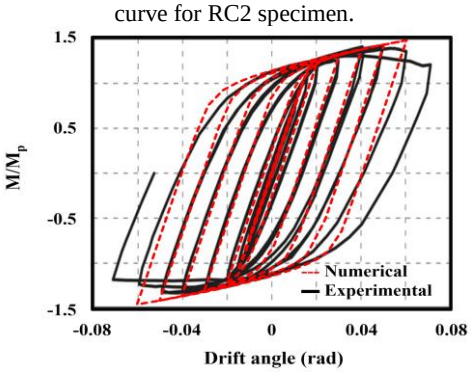

Fig. 8: Experimental [20] and numerical moment-drift angle curve for RC4 specimen.

This whole pre-modeling process was to make sure that the results of later FEA procedures are reliable, and as it appears, the selection of material properties and elements will lead to relatively accurate results.

3. Finite element models

3.1. Top and seat angle (TSA) connections

Rough details for finite element models of TSA connections are presented in Figure 9.

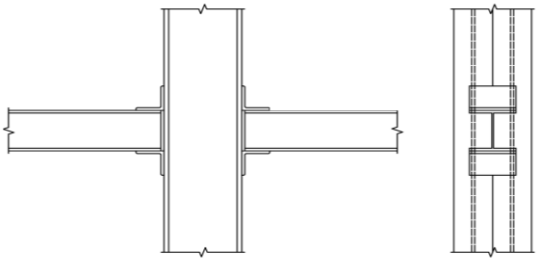

Fig. 9: Cross-shaped setup for top and seat angle (TSA) connections.

In this setup, all models had columns of 3m in length, and the gap between the beam and column was kept constant at 20 mm. Angles are connected to beam and column using fillet welds at each flange. These specimens are created according to descriptions in Eurocode [22]. Meshing was done using the C3D20 element for angles, C3D8 for beams and columns, and C3D15 for welds and fillet areas of angles. A sample finite element model is shown in Figure 10.

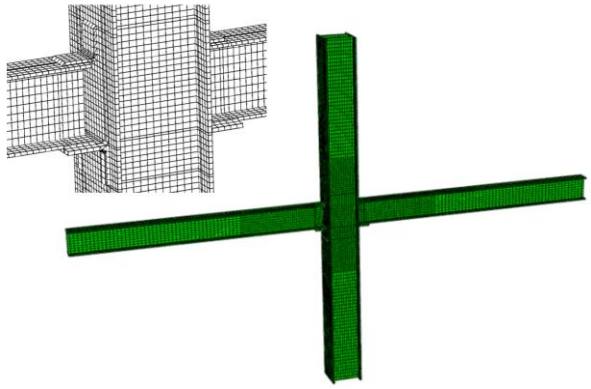

Fig. 10: Sample finite element model of top and seat angle (TSA) connection.

To determine the effects of geometric parameters on flexural performance of top and seat angle connection, a total of 34 specimens were modeled and analyzed. Details of each specimen are included in Table 2 below.

3.2. Stiffened welded-seat connections (SWS)

The schematics for finite element models of the SWS connections are illustrated in Figure 11.

Table 2: Details and dimensions of finite element models of top and seat angle (TSA) connections (dimensions are in millimeters).

Specimen ID	Beam section	Column section	Seat angle section	Seat angle length	Top angle section	Top angle length	Seat angle weld leg	Top angle weld leg
TSA-01	IPE160 L=2000 mm	2IPE180	100×100×10	100	60×60×6	40	6	6
TSA-02						50		
TSA-03					60×60×8	60		
TSA-04								
TSA-05					60×60×10			
TSA-06					80×80×8			
TSA-07					100×100×8			
TSA-08	IPE180 L=2000 mm	2IPE200	100×100×10	120	70×70×7	60	7	7
TSA-09						70		
TSA-10					70×70×9	80		
TSA-11								
TSA-12					70×70×11			
TSA-13					75×75×7			
TSA-14					80×80×7			
TSA-15	IPE200 L=2000 mm	2IPE240	100×100×10	150	80×80×8	60	8	8
TSA-16						70		
TSA-17					80×80×10	80		
TSA-18								
TSA-19					80×80×12			
TSA-20					100×100×12			
TSA-21					120×120×12			
TSA-22	IPE240 L=2500 mm	2IPE270	120×120×12	160	80×80×8	80	8	8
TSA-23						90		
TSA-24					80×80×10	100		
TSA-25								
TSA-26					80×80×12			
TSA-27					100×100×12			
TSA-28					120×120×12			
TSA-29	IPE240 L= 2500 mm	2IPE270	120×120×12	170	80×80×8	100	8	8
TSA-30								
TSA-31			120×120×13	180				
TSA-32			120×120×15					
TSA-33			130×130×12					
TSA-34			150×150×12					

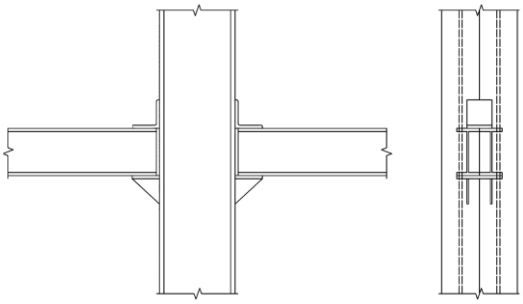

Fig. 11: Cross-shaped setup for stiffened welded-seat (SWS) connections.

In all specimens, columns are 3 meters, and weld leg length is 8 millimeters. The gap between columns and beams is not constant. Meshing on the bottom plate was done using the C3D15 element, and for other parts, it is similar to top and seat angle connection specimens. A sample finite element model of this connection is presented in Figure 12.

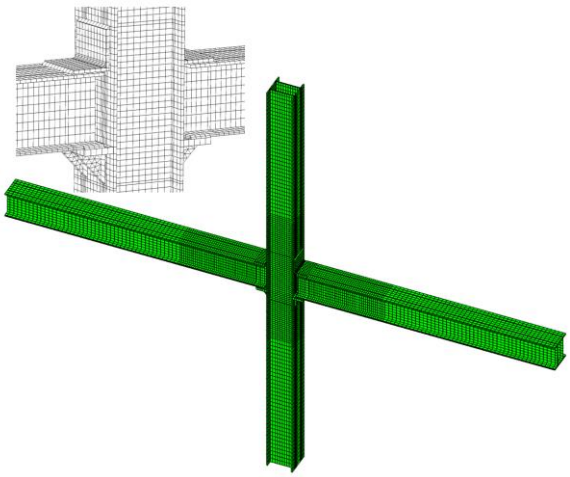

Fig. 12: Sample finite element model of stiffened welded-seat connection.

Table 3: Details and dimensions of finite element models of stiffened welded-seat (SWS) connections (dimensions are in millimeters)

Specimen ID	Beam section	Column section	Clap angle section		Triangular stiffener	Seat plate	The gap between beams and columns
SWS-01	2IPE180	2IPE200	100×100×10	150	80×80×10	200×80×16	24
SWS-02					80×80×12		
SWS-03					80×80×15		
SWS-04	2IPE240	2IPE270	100×100×10	200	100×100×16	270×100×22	20
SWS-05					100×100×18		
SWS-06					100×100×20		
SWS-07	2IPE180	2IPE200	100×100×10	150	80×70×10	200×70×12	24
SWS-08					80×80×10	200×80×12	
SWS-09					80×90×10	200×90×12	
SWS-10	2IPE240	2IPE270	100×100×10	200	100×90×18	270×90×20	20
SWS-11					100×100×18	270×100×20	
SWS-12					100×110×18	270×110×20	
SWS-13	2IPE180	2IPE200	100×100×10	150	90×80×10	200×80×12	24
SWS-14					100×80×10		
SWS-15	2IPE240	2IPE270	100×100×10	200	100×100×16	270×100×18	20
SWS-16					110×100×16		
SWS-17					120×100×16		
SWS-18	2IPE180	2IPE200	100×100×10	150	80×80×10	200×80×10	24
SWS-19						200×80×15	
SWS-20	2IPE240	2IPE270	100×100×10	200	100×100×16	270×100×16	20
SWS-21						270×100×20	
SWS-22	2IPE180 L=2000	2IPE200 L=3000	100×100×8	140	80×80×10	200×80×12	24
SWS-23			100×100×10				
SWS-24			100×100×12				
SWS-25			100×100×10	130			
SWS-26			110×110×12	140			
SWS-27			120×120×12				
SWS-28	2IPE240 L=2500	2IPE270 L=3000	100×100×8	190	100×100×16	270×100×18	20
SWS-29			100×100×10				
SWS-30			100×100×12				
SWS-31			100×100×10	180			
SWS-32			110×110×12	190			
SWS-33			120×120×12				

A total of 33 connection specimens were modeled and analyzed. Details and geometric information for each specimen are included in Table 3.

4. Analytical models

Chisala's model is expressed in a general form, therefore, it can be used to determine the moment-rotation curve for any type of steel connection. This fact is beneficial for researchers, but there is a very important issue. To use this model to its full potential, and determine the necessary parameters, a relatively precise equivalent analytical model of the connection should be created. This procedure is explained in further sections.

4.1. Top and seat angle connections

According to results obtained by Azizinamini et al. [14], seat angle does not contribute to the initial stiffness of the connection, significantly, and the beam tends to rotate around its lower flange. Since the beam has relatively a huge stiffness, it can be considered as a rigid component. These facts were used to create the equivalent analytical model for top and seat angle connections. This model is presented in Figure 13.

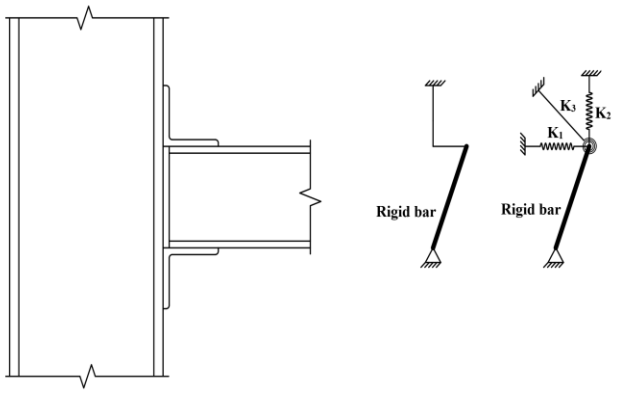

Fig. 13: The equivalent analytical model with stiffness components for top and seat angle connections.

In this model, K_1, K_2, and K_3 represent stiffness components of the top angle. The beam is considered as a rigid bar, and the hinge at the bottom is the seat angle. A matrix analysis program written in MATLAB was used to carry out the analysis and calculate each parameter. K_1 and K_2 are obtained as:

$$MK_1 = K_2 = \frac{15Eb_t t_t^3}{24\,(L_t - t_t/2)^3} \tag{2}$$

Where b_t, t_t, and L_t are width, thickness, and length of the top angle flange, respectively.

K_3 on the other hand is obtained as:

$$K_3 = \frac{7Eb_t t_t^3}{24(L_t - t_t/2)} \tag{3}$$

It should be mentioned that while calculating K_1, K_2, and K_3 axial and shearing deformations are not considered. The initial rotational stiffness (K_i') is:

$$K_i' = K_1 h_b^2 + K_2 (L_t - c)^2 + K_3 \tag{4}$$

Where h_b is beam section height, and c is the gap between the column and beams. By substitution of K_1, K_2, and K_3 in Eq.(4), and considering that c = 20 mm the following equation is obtained:

$$K_i' = \frac{Eb_t t_t^3}{24(L_t - t_t/2)^3} \\ [15(h_b^2 + (L_t - 20)^2) + 7(L_t - t_t/2)^2] \tag{5}$$

There is a flaw in the above equation. As the top angle flange thickness increases, Eq.(5) yields very large initial stiffness values, compared to FEA results. This is caused by the fact that fillet weld connecting the top angle vertical flange to the column is considered as fixed support in the analytical model. When the weld leg is equal to the top angle flange thickness, Eq.(5) yields acceptable values, and the fixed support assumption becomes true, but as the top angle flange thickness increases, this assumption becomes more unreliable. To fix this issue, assuming that the relation between the initial stiffness of the connection, and weld leg to top angle thickness ratio (a_w/t_t) is linear, the initial stiffness can be reduced to:

$$K_i = K_i' \frac{a_w}{t_t} = \frac{Eb_t t_t^2 a_w}{24(L_t - t_t/2)^3} \\ [15(h_b^2 - 20)^2 + 7(L_t - t_t/2)^2] \tag{6}$$

where a_w is the fillet weld leg.

The plastic stiffness (K_p) can be considered as a function of the initial stiffness (K_i), which is obtained using linear regression analysis:

$$K_p = 0.223(K_i)^{0.85} \tag{7}$$

The regression analysis diagram is presented in Figure 14.

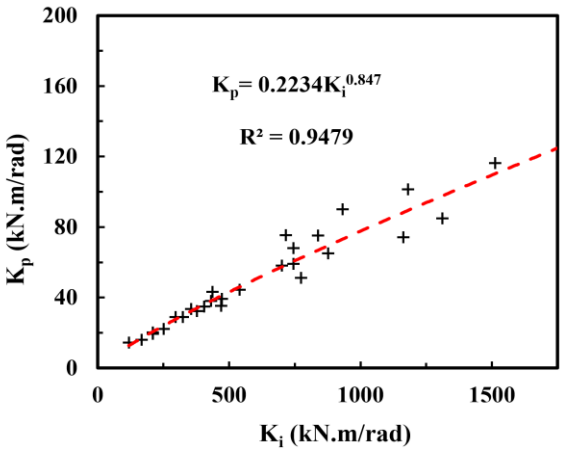

Fig. 14: Regression analysis diagram.

Using another linear regression analysis, the intercept-constant (M_0) becomes:

$$M_0 = 27 \times 10^{-6}(b_t)^{0.66}(t_t)^{0.87}(L_t)^{-0.23}(h_b)^{1.54} \quad (8)$$

4.2. Stiffened welded-seat connections

Similar to top and seat angle connections, the main aspect of flexural performance of the stiffened welded-seat connections is the beam's tendency to rotate around the seat components. This is prevented mostly by the stiffened seat, which causes beam flange uplift. This matter is shown in Figure 15.

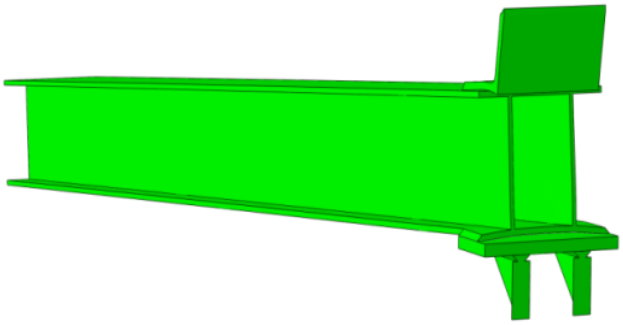

Fig. 15: Beam flange uplift under bending moment.

The equivalent analytical model for stiffened welded-seat connections is similar to the previous section with a slight modification. This model is presented in Figure 16.

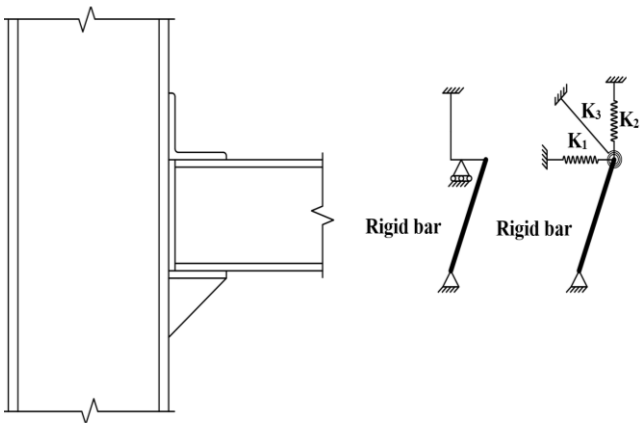

Fig. 16: The equivalent analytical model with stiffness components for stiffened welded-seat connections.

Each of K_1, K_2, and K_3 can be calculated using the following equations derived using matrix structural analysis program written in MATLAB:

$$K_1 = \frac{Eb_t t_t^3(3L_1+5L_2)}{(3L_1+8L_2)(L_1+L_2)^3} \quad (9)$$

$$K_2 = \frac{Eb_t t_t^3(2L_1 + BL_1L_2 + 3L_1^2)}{L_1^3(3L_1 + 8L_2)(L_1 + L_2)} \quad (10)$$

$$K_3 = \frac{Eb_t t_t^3(6L_2^2 + 10L_1L_2 + 3L_1^2)}{3L_1(3L_1 + 8L_2)(L_1 + L_2)} \quad (11)$$

In the above equations b_t, t_t, and L_2 are the thickness and width of the top angle flange, and the gap between the beam and the column, respectively ($L_1 = L_t - L_2$ and L_t is top angle length). By calculating K_1, K_2, and K_3 using the equations above, the initial rotational stiffness (K_i') becomes:

$$K_i = [K_1 h_b^2 + K_2 L_2^2 + K_3]\frac{a_w}{t_t} \quad (12)$$

where h_b, and a_w are beam section height, and fillet weld leg (weld connecting the vertical flange of the top angle to the column). Same as the previous section, linear regression analysis was used to determine the plastic stiffness (K_p) as a function of initial stiffness (K_i), which yielded:

$$K_p = 0.11(K_i)^{0.89} \quad (13)$$

The linear regression diagram is illustrated in Figure 17.

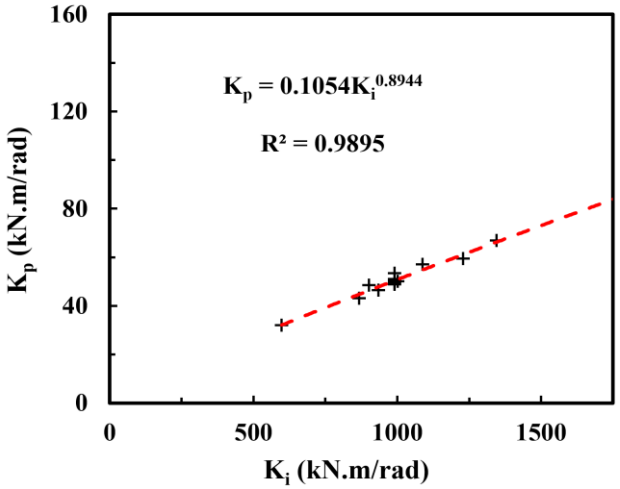

Fig. 17: Regression analysis diagram.

The intercept-constant (M_0) is obtained from linear regression analysis same as the previous section:

$$M_0 = 83.2 \times 10^{-6}(b_t)^{0.29}(t_t)^{0.97}(L_t)^{e-0.76}(L_p)^{0.16}(h_b)^2 \quad (14)$$

wher L_p is the largest dimension of the triangular stiffener plate.

5. Results and discussion

In this section, the analytical and numerical results along with moment-rotation curves for both specimen series are provided.

5.1. Top and seat angle connections

The analytical and numerical results for top and seat angle (TSA) connection specimens are presented in Table 4.

Table 4: Analytical and numerical results for TSA specimens.

Specimen ID	K_i (kN.m/rad)		K_p (kN.m/rad)		M_0 (kN.m)	
	(Analytical)	(Abaqus)	(Analytical)	(Abaqus)	(Analytical)	(Abaqus)
TSA-01	167.40	217.47	17.30	16.10	1.40	1.45
TSA-02	209.40	257.65	20.70	19.50	1.60	1.65
TSA-03	251.20	297.93	24.10	22.30	1.90	1.85
TSA-04	470.10	511.49	41.10	35.40	2.40	2.45
TSA-05	773.80	774.44	62.80	51.10	2.90	2.80
TSA-06	209.30	291.78	20.70	20.20	2.20	2.24
TSA-07	118.20	193.77	12.70	14.50	2.10	2.15
TSA-08	323.40	371.04	29.90	29.01	2.40	2.45
TSA-09	377.30	421.76	34.10	32.30	2.70	2.65
TSA-10	431.20	471.93	38.20	38.10	3.00	3.00
TSA-11	744.60	795.01	60.80	59.10	3.70	3.85
TSA-12	1162.90	1169.81	88.70	74.20	4.40	4.50
TSA-13	354.80	414.19	32.40	33.50	2.90	2.95
TSA-14	296.70	363.47	27.80	28.90	2.90	2.90
TSA-15	405.00	417.64	36.20	35.00	3.10	3.20
TSA-16	472.40	466.48	41.30	39.20	3.50	3.55
TSA-17	539.90	521.69	46.20	44.50	3.80	3.90
TSA-18	876.50	772.36	69.80	65.00	4.60	4.65
TSA-19	1312.10	1074.24	98.30	85.00	5.40	5.50
TSA-20	700.80	729.59	57.70	58.10	5.10	5.30
TSA-21	435.90	517.91	38.50	43.20	4.90	5.05
TSA-22	745.20	753.36	60.80	68.00	5.00	5.10
TSA-23	838.40	831.43	67.20	75.10	5.40	5.55
TSA-24	931.60	911.24	73.50	90.00	5.80	6.00
TSA-25	1513.00	1391.26	111.00	116.20	7.10	7.30
TSA-26	2265.60	1943.90	156.40	148.00	8.30	8.20
TSA-27	1181.00	1267.20	89.90	101.30	7.90	7.80
TSA-28	716.00	836.99	58.80	75.40	7.50	7.30
TSA-29	931.60	906.37	74.50	76.00	5.80	5.60
TSA-30	931.60	909.71	74.50	76.10	5.80	5.65
TSA-31	931.60	916.39	74.50	76.30	5.80	5.70
TSA-32	931.60	973.93	74.50	80.00	5.80	5.80
TSA-33	931.60	923.71	74.50	77.00	5.80	5.72
TSA-34	931.60	934.60	74.50	78.50	5.80	5.74

As it appears, Chisala's model can precisely determine the parameters necessary to plot the moment-rotation curve for top and seat angle connections. Based on the obtained data, the analytical and numerical moment-rotation curves for TSA specimens were plotted. Figure 18. to Figure 51. below, present these curves for specimens TSA-01 to TSA-34.

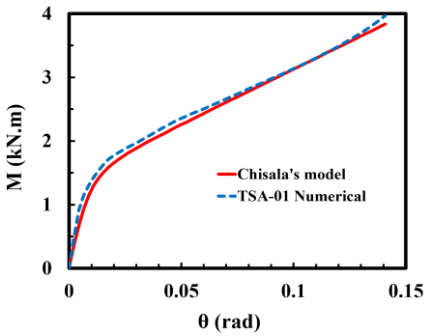

Fig. 18: Numerical and analytical moment-rotation curves for TSA-01 specimen.

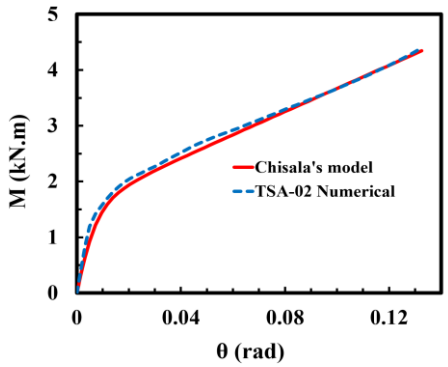

Fig. 19: Numerical and analytical moment-rotation curves for TSA-02 specimen.

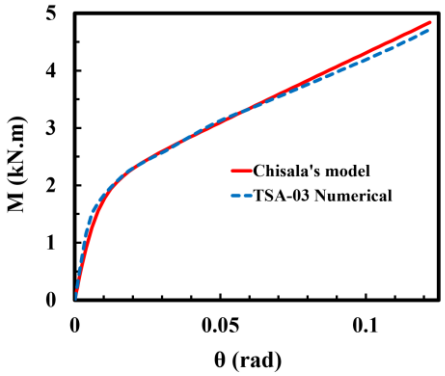

Fig. 20: Numerical and analytical moment-rotation curves for TSA-03 specimen.

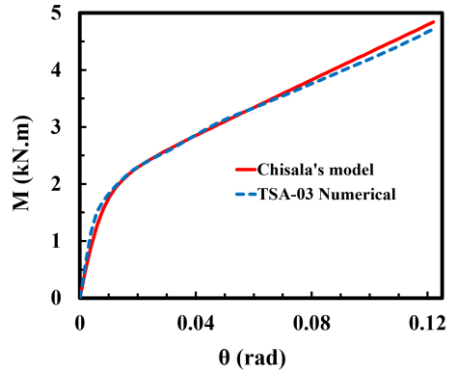

Fig. 21: Numerical and analytical moment-rotation curves for TSA-04 specimen.

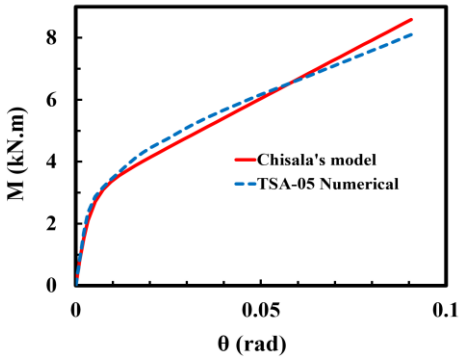

Fig. 22: Numerical and analytical moment-rotation curves for TSA-05 specimen.

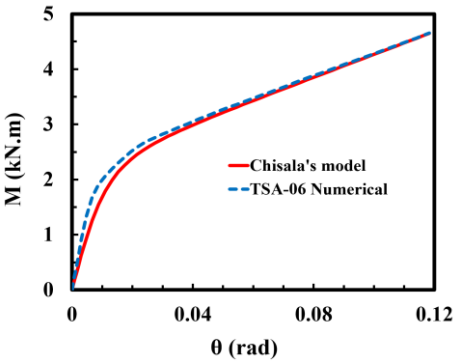

Fig. 23: Numerical and analytical moment-rotation curves for TSA-06 specimen.

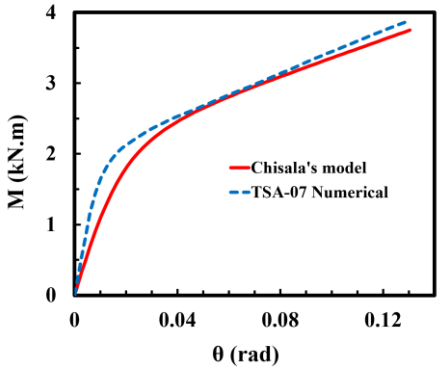

Fig. 24: Numerical and analytical moment-rotation curves for TSA-07 specimen.

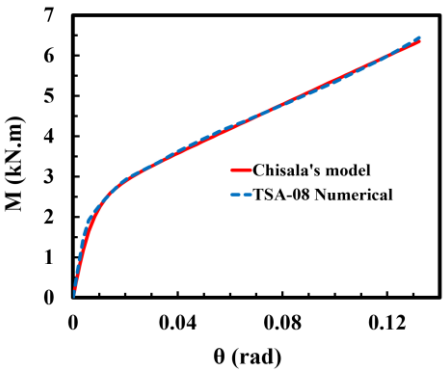

Fig. 25: Numerical and analytical moment-rotation curves for TSA-08 specimen.

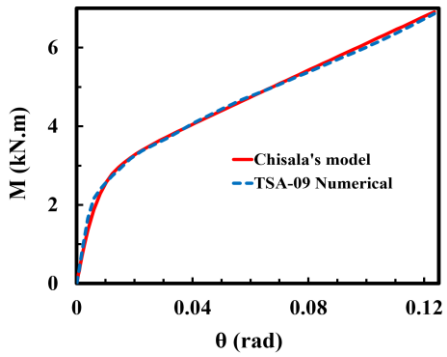

Fig. 26: Numerical and analytical moment-rotation curves for TSA-09 specimen.

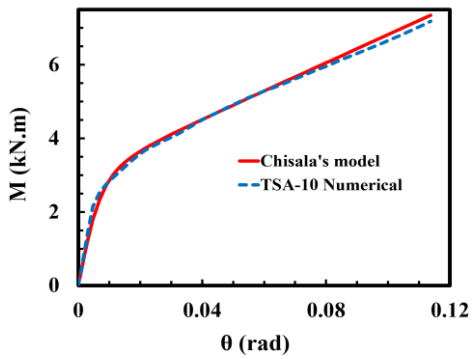

Fig. 27: Numerical and analytical moment-rotation curves for TSA-10 specimen.

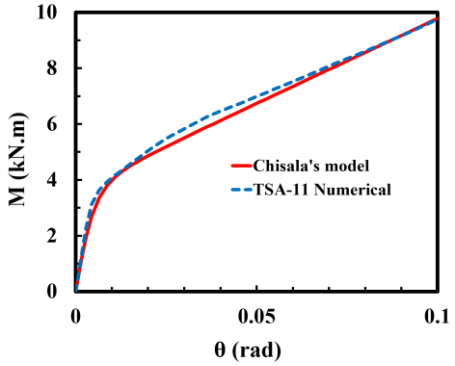

Fig. 28: Numerical and analytical moment-rotation curves for TSA-11 specimen.

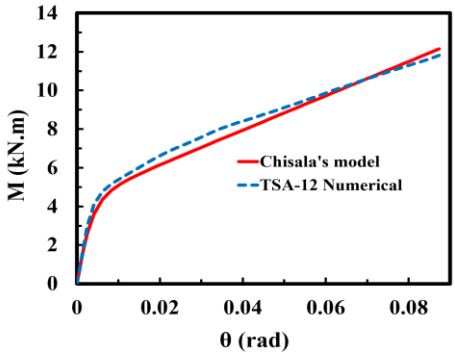

Fig. 29: Numerical and analytical moment-rotation curves for TSA-12 specimen.

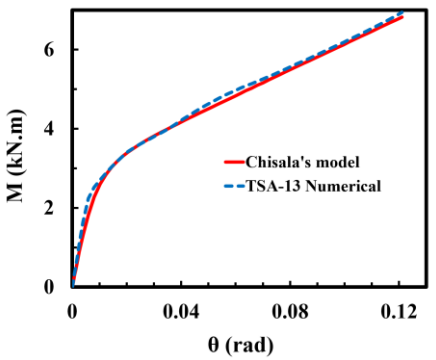

Fig. 30: Numerical and analytical moment-rotation curves for TSA-13 specimen.

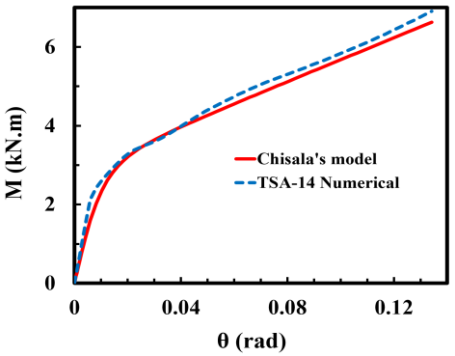

Fig. 31: Numerical and analytical moment-rotation curves for TSA-14 specimen.

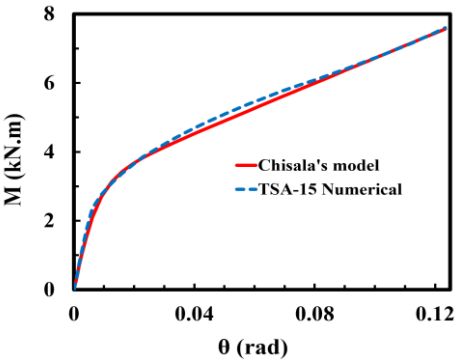

Fig. 32: Numerical and analytical moment-rotation curves for TSA-15 specimen.

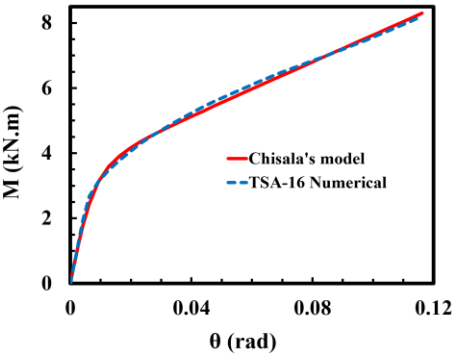

Fig. 33: Numerical and analytical moment-rotation curves for TSA-16 specimen.

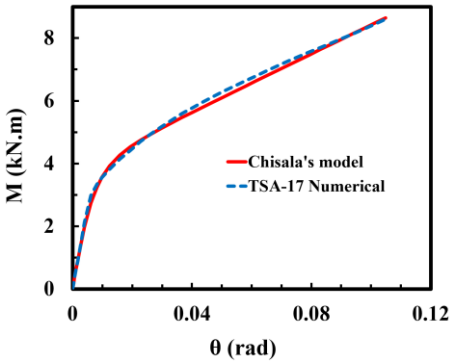

Fig. 34: Numerical and analytical moment-rotation curves for TSA-17 specimen.

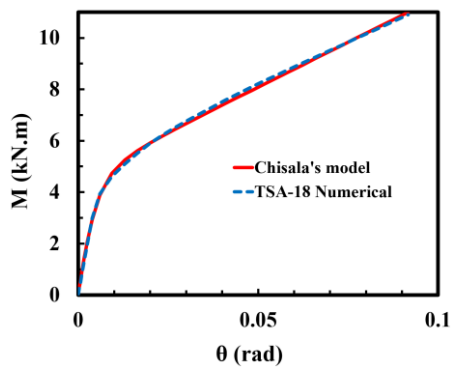

Fig. 35: Numerical and analytical moment-rotation curves for TSA-18 specimen.

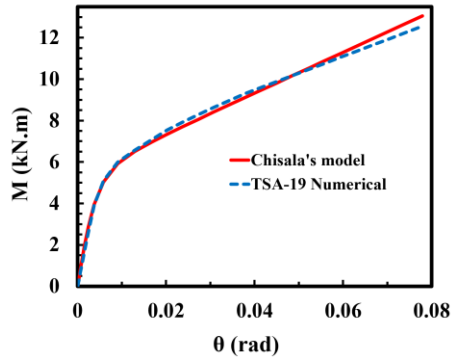

Fig. 36: Numerical and analytical moment-rotation curves for TSA-19 specimen.

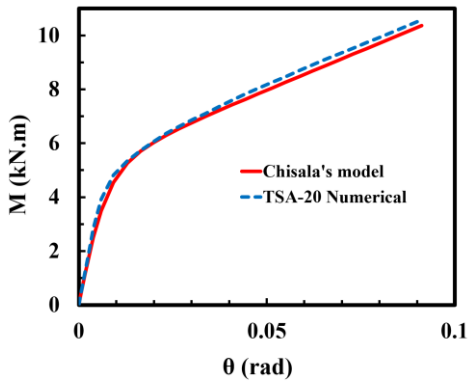

Fig. 37: Numerical and analytical moment-rotation curves for TSA-20 specimen.

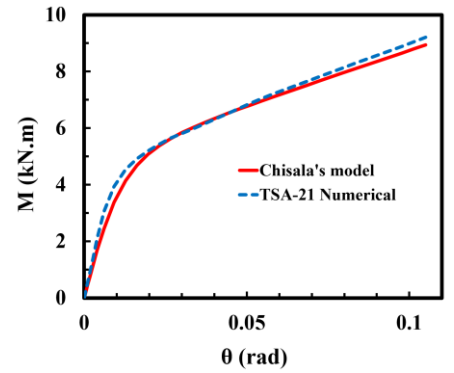

Fig. 38: Numerical and analytical moment-rotation curves for TSA-21 specimen.

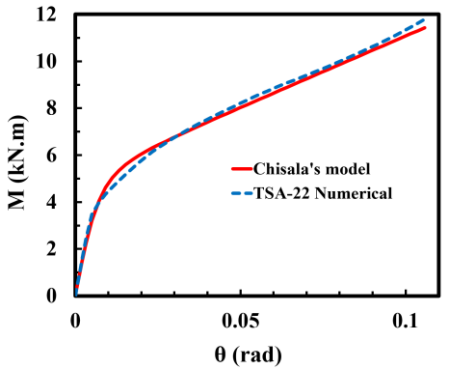

Fig. 39: Numerical and analytical moment-rotation curves for TSA-22 specimen.

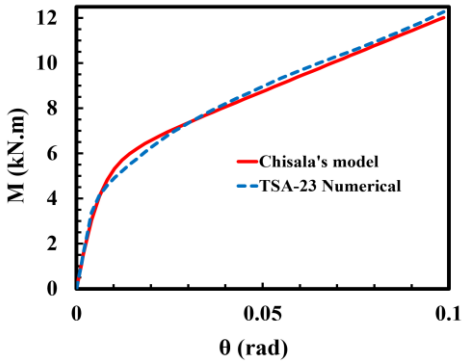

Fig. 40: Numerical and analytical moment-rotation curves for TSA-23 specimen.

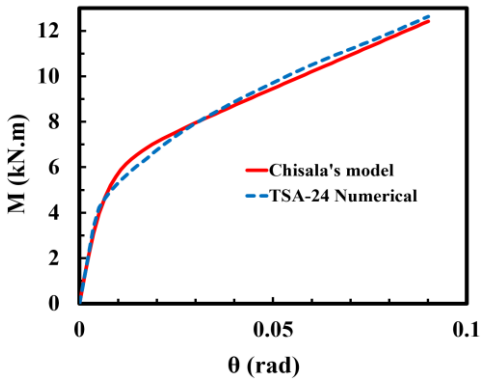

Fig. 41: Numerical and analytical moment-rotation curves for TSA-24 specimen.

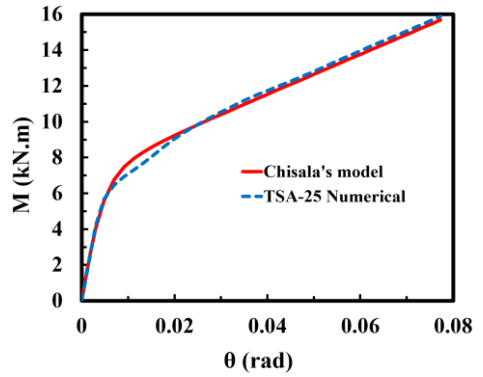

Fig. 42: Numerical and analytical moment-rotation curves for TSA-25 specimen.

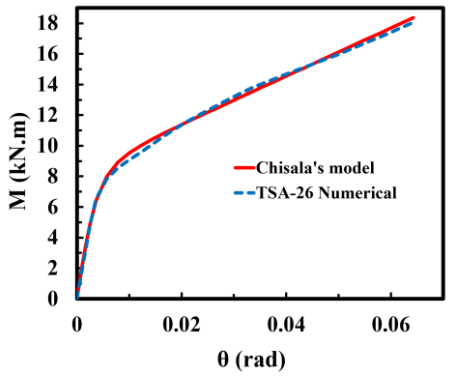

Fig. 43: Numerical and analytical moment-rotation curves for TSA-26 specimen.

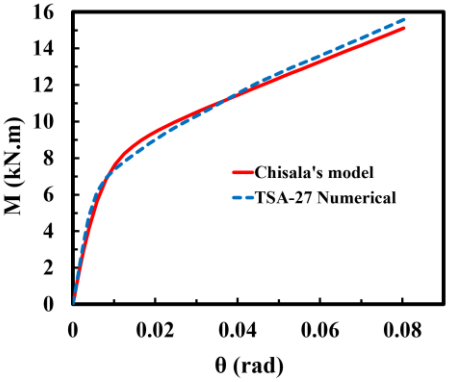

Fig. 44: Numerical and analytical moment-rotation curves for TSA-27 specimen.

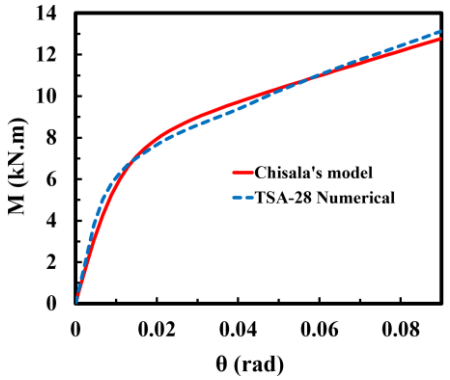

Fig. 45: Numerical and analytical moment-rotation curves for TSA-28 specimen.

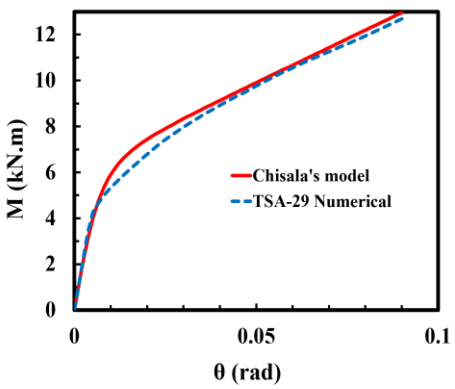

Fig. 46: Numerical and analytical moment-rotation curves for TSA-29 specimen.

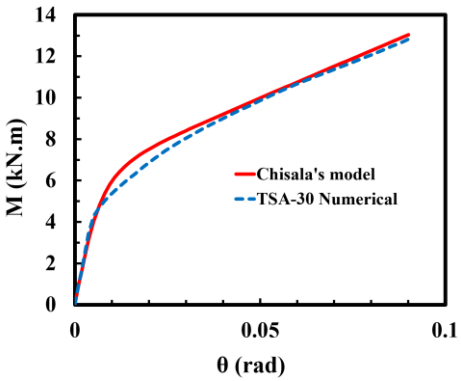

Fig. 47: Numerical and analytical moment-rotation curves for TSA-30 specimen.

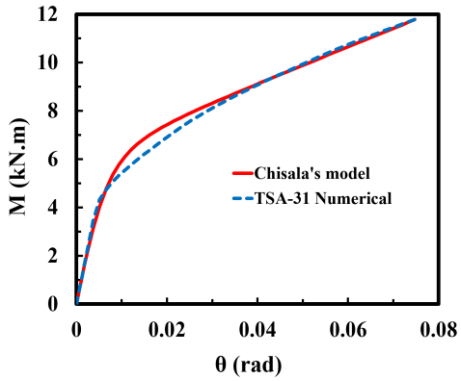

Fig. 48: Numerical and analytical moment-rotation curves for TSA-31 specimen.

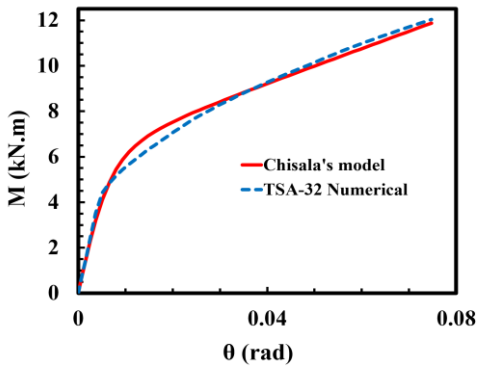

Fig. 49: Numerical and analytical moment-rotation curves for TSA-32 specimen.

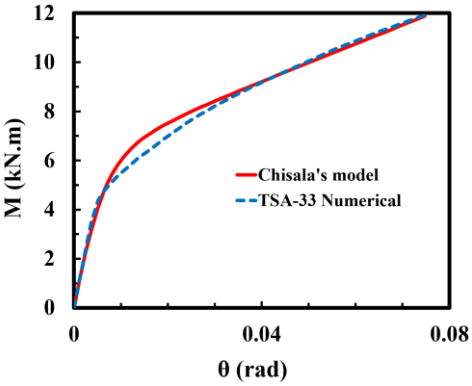

Fig. 50: Numerical and analytical moment-rotation curves for TSA-33 specimen.

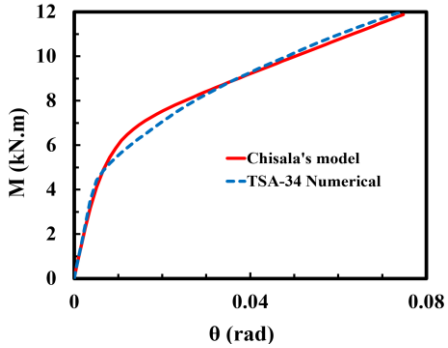

Fig. 51: Numerical and analytical moment-rotation curves for TSA-34 specimen.

As it is presented in previous figures, it is clear that Chisala's model can precisely predict the moment-rotation curve for top and seat angle connections, and as it is easy to utilize, it can be used to provide better vision for structural engineers on the performance of these connections as well. The comparison between the analytical and numerical moment-rotation curves for top and seat angle connections reveals that these connections exhibit a semi-rigid flexural performance. There are other results derived from the comparisons that are described in further sections.

5.1.1. Effects of the top angle length

Changing the top angle length has a direct effect on the initial and plastic stiffness. This claim can be confirmed by comparing the specimens. For instance, increasing the top angle length from 40 mm to 50 mm in TSA-01 and TSA-02 increases the initial and plastic stiffness by 19%, and 21%, respectively. Figure 52. to Figure 55., present these effects.

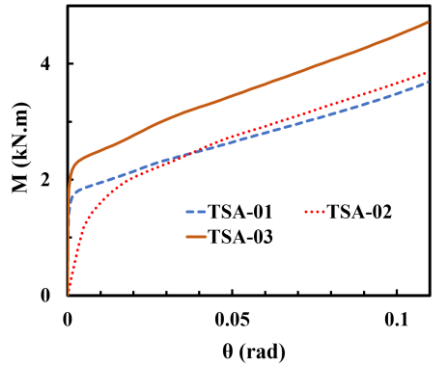

Fig. 52: Top angle length effects on the moment-rotation curve.

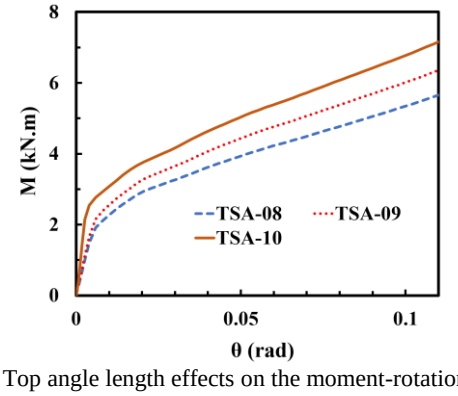

Fig. 53: Top angle length effects on the moment-rotation curve.

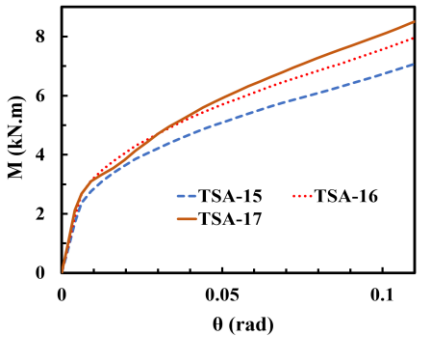

Fig. 54: Top angle length effects on the moment-rotation curve.

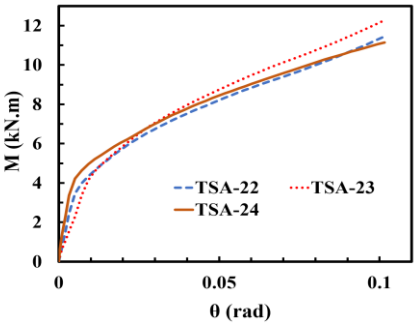

Fig. 55: Top angle length effects on the moment-rotation curve.

5.1.2. Effects of the top angle thickness

Variations of the top angle thickness have a significant direct effect on the initial, and plastic stiffness values. As an example, changing the thickness from 7 mm to 9 mm in TSA-10 and TSA-11 specimens increases the initial, and plastic stiffness by 68%, and 60%, respectively. The following figures (Figure 56. To Figure 59.) present the comparison between the moment-rotation curves for TSA specimens with varying top angle thickness.

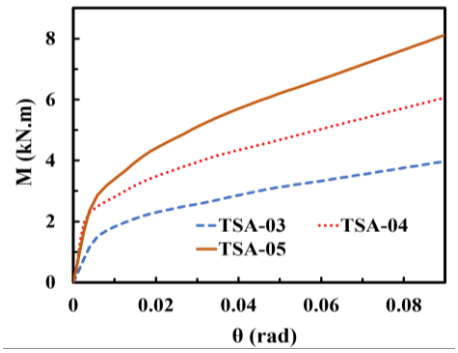

Fig. 56: Top angle thickness effects on the moment-rotation curve.

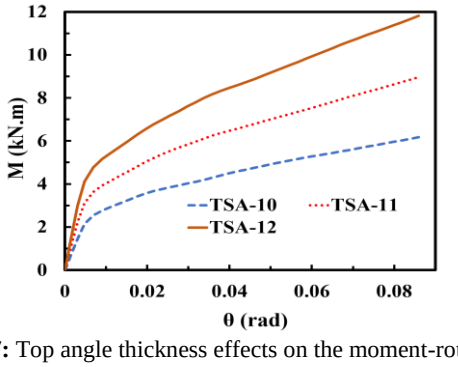

Fig. 57: Top angle thickness effects on the moment-rotation curve.

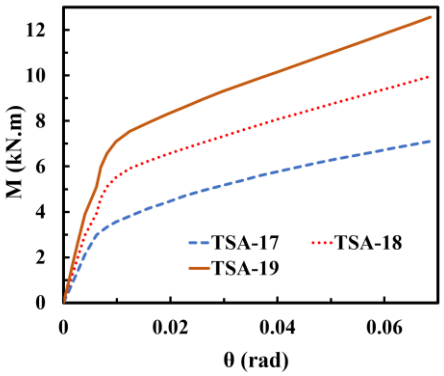

Fig. 58: Top angle thickness effects on the moment-rotation curve.

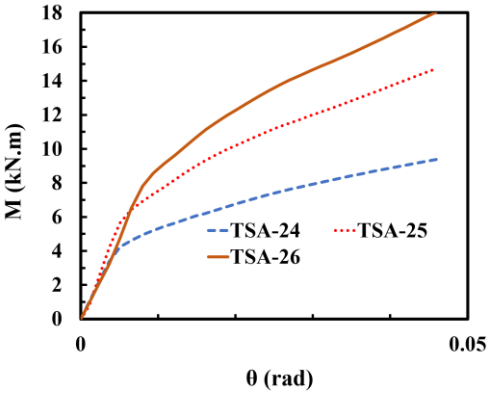

Fig. 59: Top angle thickness effects on the moment-rotation curve.

5.1.3. Effects of the top angle flange length

Unlike the previous sections, the top angle flange length is in a reverse relation with the initial, and plastic stiffness values. For example, comparing TSA-20 and TSA-21 specimens reveals that increasing the top angle flange thickness from 100 mm to 120 mm decreases the initial, and plastic stiffness values by 29%, and 26%, respectively. The following figures (Figure 60. to Figure 63.) indicate the comparison between the moment-rotation curves regarding this matter.

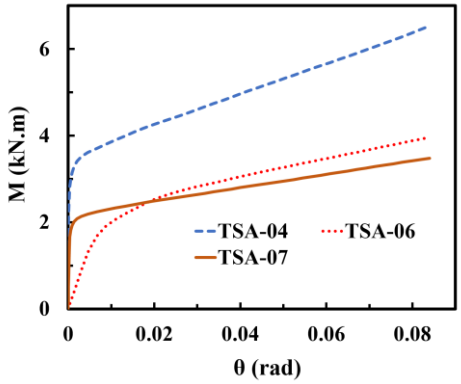

Fig. 60: Top angle flange length effects on the moment-rotation curve.

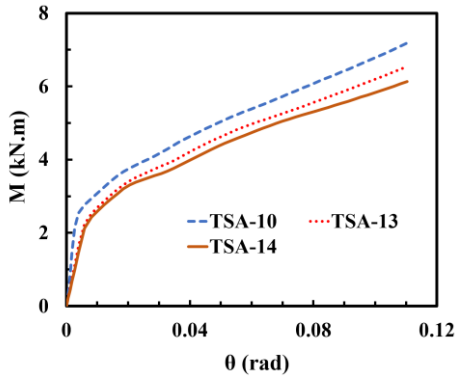

Fig. 61: Top angle flange length effects on the moment-rotation curve.

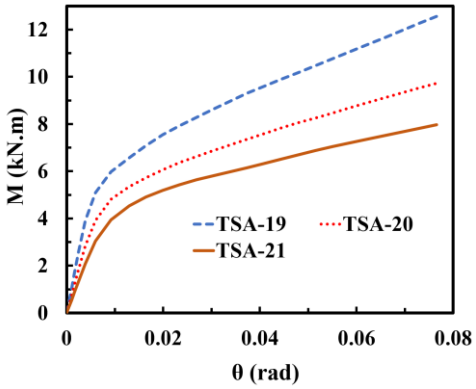

Fig. 62: Top angle flange length effects on the moment-rotation curve.

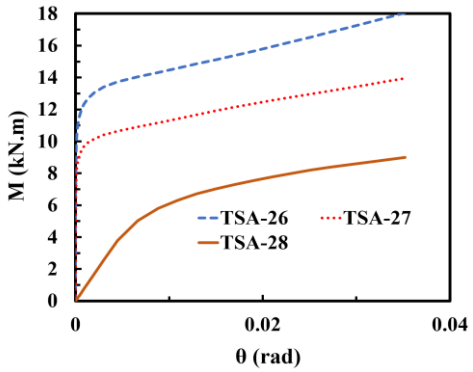

Fig. 63: Top angle flange length effects on the moment-rotation curve.

5.1.4. Effects of the seat angle dimensions

As the seat angle has larger dimensions than the top angle, it has more stiffness, therefore, it acts as fixed support allowing the beam to rotate around its lower flange, which causes the top angle to carry most of the subjected load. This fact renders the effects of the seat angle dimensions on the performance of the connection rather insignificant, and negligible.

5.2. Stiffened welded-seat connections

The analytical and numerical results for stiffened welded-seat (SWS) connection specimens are contained in Table 5.

Table 5: Analytical and numerical results for SWS specimens.

Specimen ID	K_i (kN.m/rad)		K_p (kN.m/rad)		M_0 (kN.m/rad)	
	(Analytical)	(Abaqus)	(Analytical)	(Abaqus)	(Analytical)	(Abaqus)
SWS-01	990.80	906.92	51.00	49.30	6.50	6.70
SWS-02	990.80	908.46	51.00	50.47	6.50	6.70
SWS-03	990.80	909.47	51.00	50.52	6.50	6.70
SWS-04	2020.10	2212.43	96.20	102.34	13.10	13.50
SWS-05	2020.10	2201.15	96.20	96.12	13.10	13.50
SWS-06	2020.10	2202.43	96.20	96.90	13.10	13.50
SWS-07	990.80	872.98	51.00	50.00	6.40	6.20
SWS-08	990.80	916.62	51.00	50.50	6.50	6.70
SWS-09	990.80	972.22	51.00	53.40	6.70	7.30
SWS-10	2020.10	2073.13	96.20	91.20	12.90	12.50
SWS-11	2020.10	2192.99	96.20	96.50	13.10	13.40
SWS-12	2020.10	2197.44	96.20	96.90	13.30	13.60
SWS-13	990.80	919.60	51.00	50.85	6.50	6.70
SWS-14	990.80	922.26	51.00	50.68	6.50	6.70
SWS-15	2020.10	2176.45	96.20	97.82	13.10	13.50
SWS-16	2020.10	2185.84	96.20	97.12	13.10	13.50
SWS-17	2020.10	2195.91	96.20	94.92	13.10	13.50
SWS-18	990.80	910.79	51.00	49.75	6.50	6.70
SWS-19	990.80	923.54	51.00	48.92	6.50	6.70
SWS-20	2020.10	2158.62	96.20	93.38	13.10	13.50
SWS-21	2020.10	2185.97	96.20	97.13	13.10	13.50
SWS-22	591.80	559.44	32.30	32.10	5.20	4.80
SWS-23	924.70	855.51	48.00	46.50	6.40	6.30
SWS-24	1331.60	1229.92	66.40	66.87	7.70	7.70
SWS-25	858.70	799.26	44.90	43.10	6.30	5.90
SWS-26	1078.40	1037.75	55.00	57.07	7.10	7.40
SWS-27	894.90	885.45	46.60	48.60	6.70	7.10
SWS-28	1228.20	1352.26	61.80	59.50	10.40	10.35
SWS-29	1919.00	2074.66	91.90	93.13	12.90	13.00
SWS-30	2763.50	2682.43	127.10	120.13	15.40	14.10
SWS-31	1818.10	1973.54	87.60	80.00	12.70	12.50
SWS-32	2189.50	2251.39	103.30	99.06	14.30	13.50
SWS-33	1778.50	1915.24	85.90	84.30	13.40	13.10

Similar to TSA specimens, Chisala's model can precisely predict the parameters necessary for plotting the moment-rotation curve for each SWS specimen. Using the obtained data, analytical and numerical moment-rotation curves for each SWS specimen were plotted. The figures below (Figure 64. To Figure 83.) present these curves for specimens SWS-01 to SWS-20 (to maintain the document length, moment-rotation curves for all of the specimens are not presented).

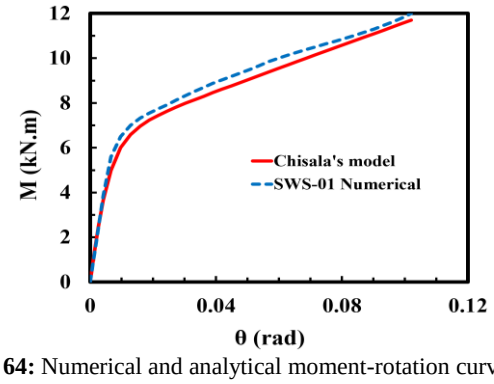

Fig. 64: Numerical and analytical moment-rotation curves for SWS-01 specimen.

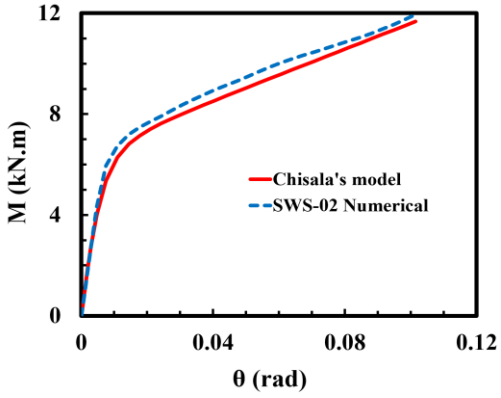

Fig. 65: Numerical and analytical moment-rotation curves for SWS-02 specimen.

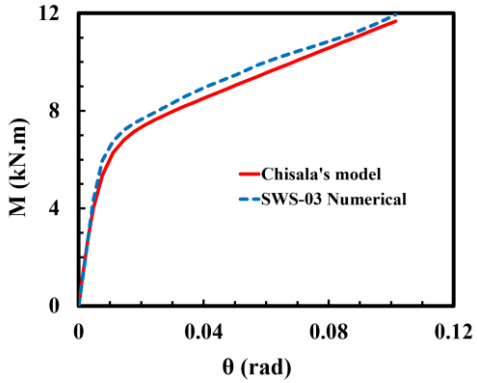

Fig. 66: Numerical and analytical moment-rotation curves for SWS-03 specimen.

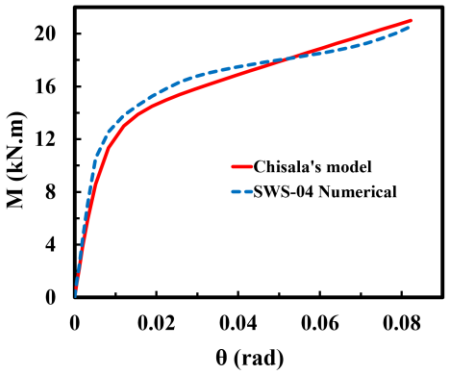

Fig. 67: Numerical and analytical moment-rotation curves for SWS-04 specimen.

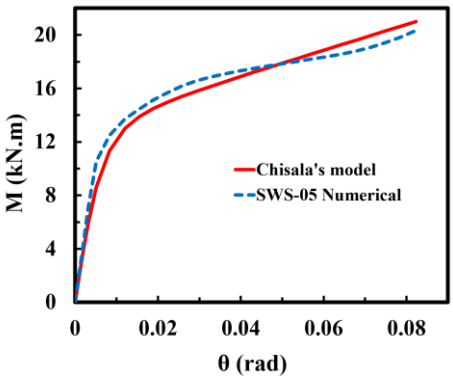

Fig. 68: Numerical and analytical moment-rotation curves for SWS-05 specimen.

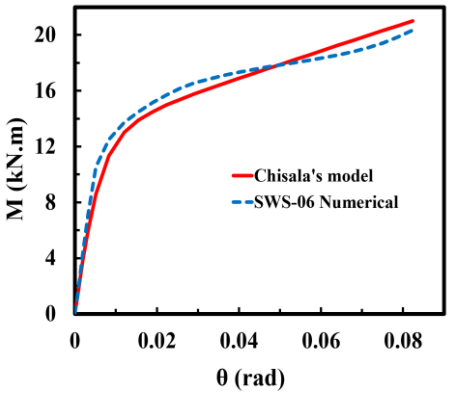

Fig. 69: Numerical and analytical moment-rotation curves for SWS-06 specimen.

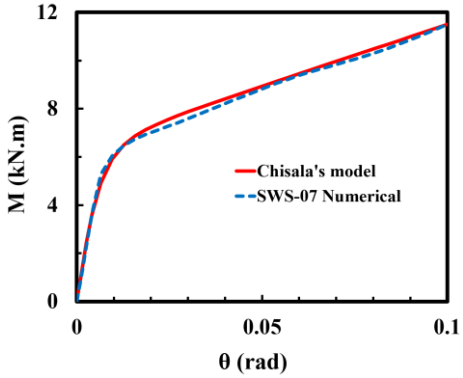

Fig. 70: Numerical and analytical moment-rotation curves for SWS-07 specimen.

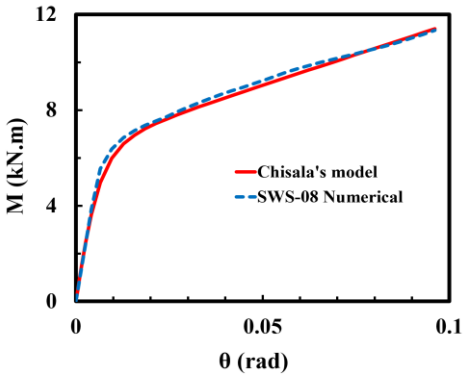

Fig. 71: Numerical and analytical moment-rotation curves for SWS-08 specimen.

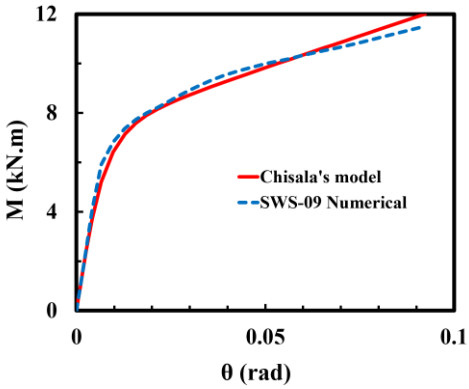

Fig. 72: Numerical and analytical moment-rotation curves for SWS-09 specimen.

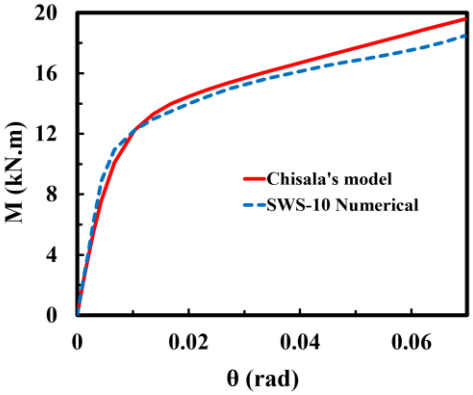

Fig. 73: Numerical and analytical moment-rotation curves for SWS-10 specimen.

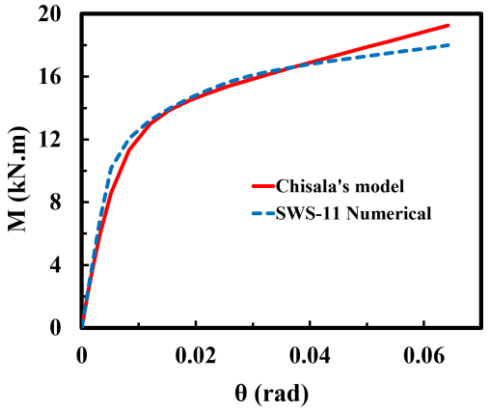

Fig. 74: Numerical and analytical moment-rotation curves for SWS-11 specimen.

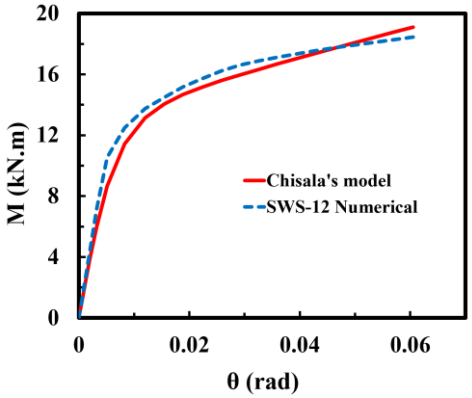

Fig. 75: Numerical and analytical moment-rotation curves for SWS-12 specimen.

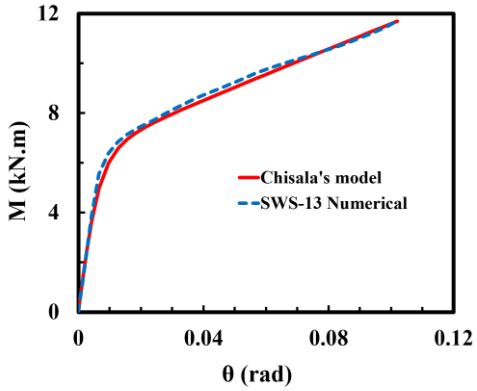

Fig. 76: Numerical and analytical moment-rotation curves for SWS-13 specimen.

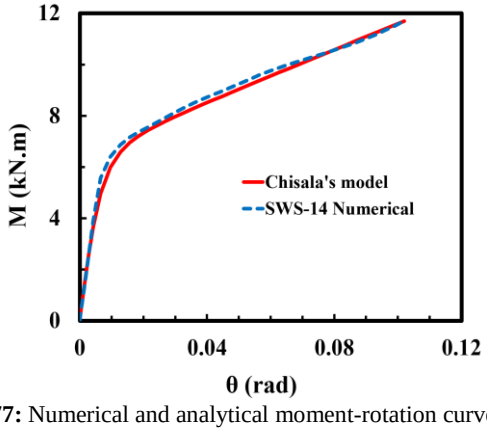

Fig. 77: Numerical and analytical moment-rotation curves for SWS-14 specimen.

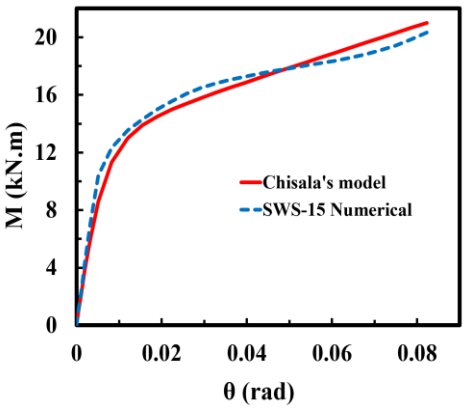

Fig. 78: Numerical and analytical moment-rotation curves for SWS-15 specimen.

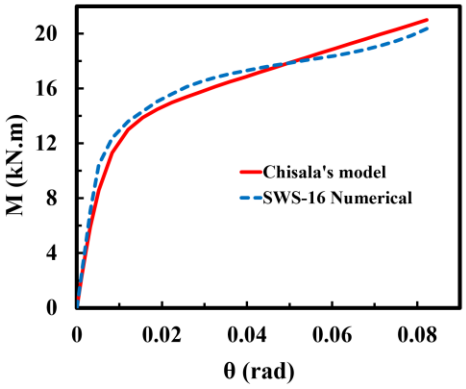

Fig. 79: Numerical and analytical moment-rotation curves for SWS-16 specimen.

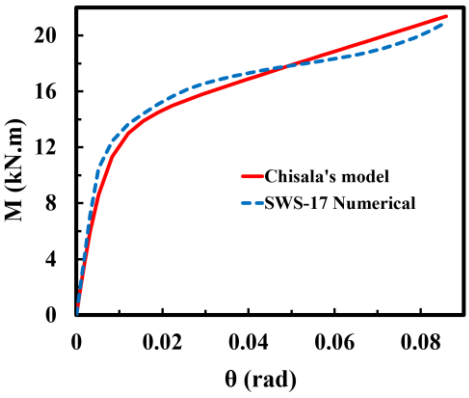

Fig. 80: Numerical and analytical moment-rotation curves for SWS-17 specimen.

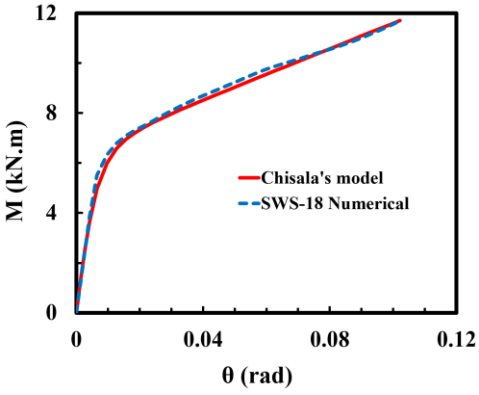

Fig. 81: Numerical and analytical moment-rotation curves for SWS-18 specimen.

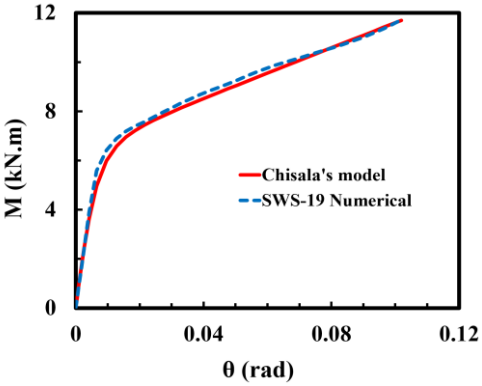

Fig. 82: Numerical and analytical moment-rotation curves for SWS-19 specimen.

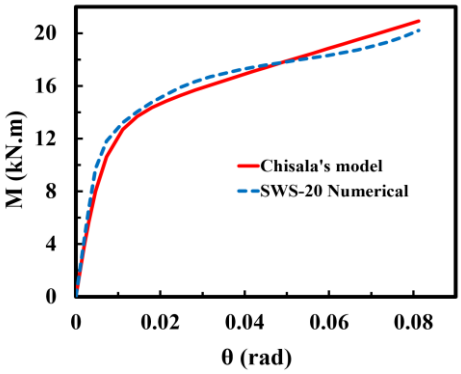

Fig. 83: Numerical and analytical moment-rotation curves for SWS-20 specimen.

As it appears, Chisala's model can predict the moment-rotation curve for stiffened welded-seat connections with acceptable precision. Both the analytical and numerical moment-rotation curves reveal that stiffened welded-seat connections demonstrate a semi-rigid flexural performance. The effects of geometric dimensions of each component on the performance of stiffened welded-seat connections are described in further sections.

5.2.1. Effects of the triangular stiffener thickness

Contrary to intuition, the thickness of the triangular stiffener plate does not affect the performance of stiffened welded-seat connections significantly. This matter is presented in Figure 84.

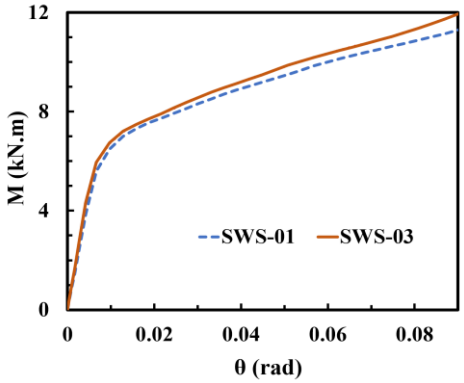

Fig. 84: Effects of the triangular stiffener thickness on the moment-rotation curve.

5.2.2. Effects of the triangular stiffener width

The width of the triangular stiffener plate does not affect the initial, and plastic stiffness, however, it has a direct and significant effect on the overall strength of stiffened welded-seat connections (the overall strength of these connections is directly related to the flexural capacity). Figure 85. and Figure 86. depict this comparison.

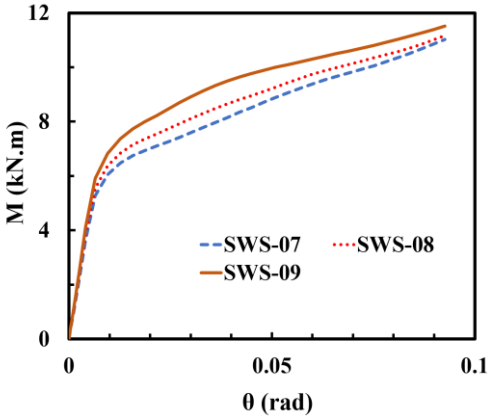

Fig. 85: Effects of the triangular stiffener width on the moment-rotation curve.

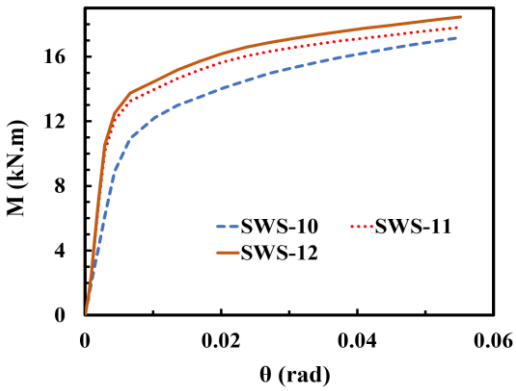

Fig. 86: Effects of the triangular stiffener width on the moment-rotation curve.

5.2.3. Effects of the seat-plate thickness

The seat-plate thickness has no significant effects on the flexural performance and the moment-rotation curve of stiffened welded-seat connections. This is shown in Figure 87.

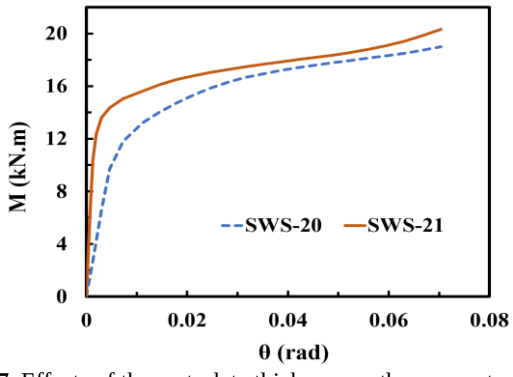

Fig. 87. Effects of the seat-plate thickness on the moment-rotation curve.

5.2.4. Effects of geometric dimensions of the top angle

Similar to top and seat angle connections, geometric dimensions of the top angle significantly affect the flexural performance of the stiffened welded-seat connections. These effects are shown in the following figures (Figure 88. to Figure 93.).

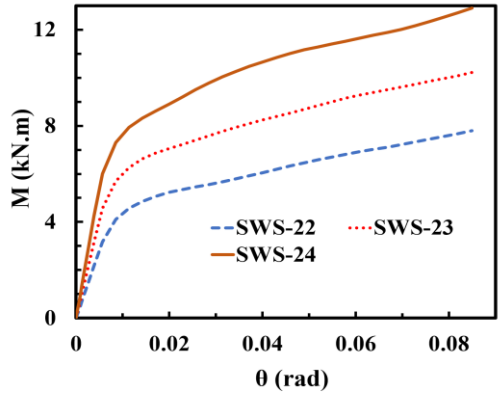

Fig. 88: Effects of top angle flange thickness on the moment-rotation curve.

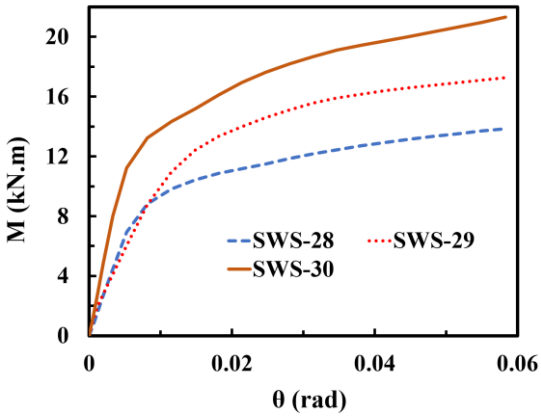

Fig. 89: Effects of top angle flange thickness on the moment-rotation curve.

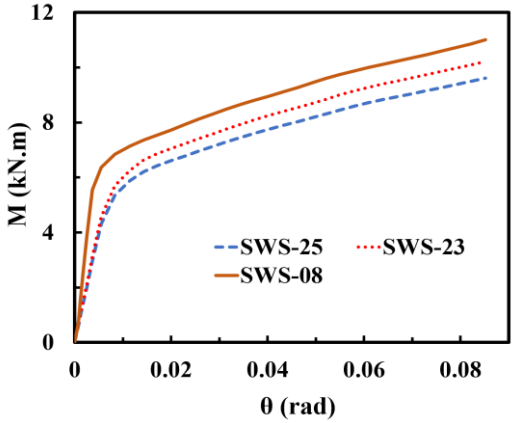

Fig. 90: Effects of top angle length on the moment-rotation curve.

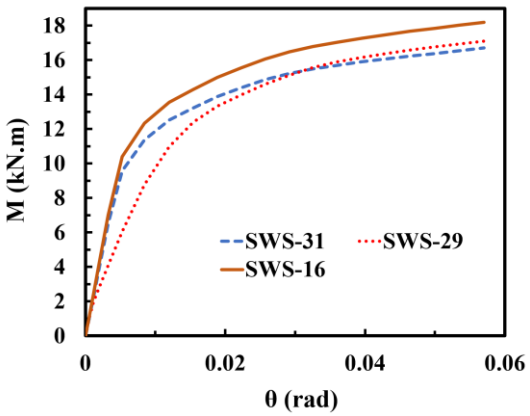

Fig. 91: Effects of top angle length on the moment-rotation curve.

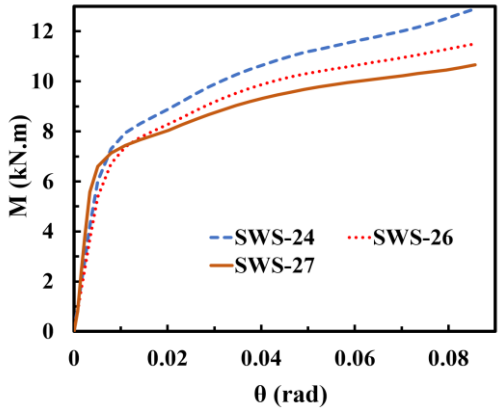

Fig. 92: Effects of top angle flange length on the moment-rotation curve.

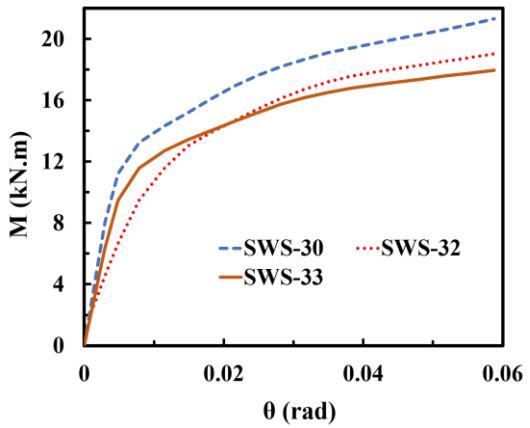

Fig. 93: Effects of top angle flange length on the moment-rotation curve

6. Conclusions

In this research, Chisala's model was used to determine the moment-rotation curve for two types of steel connections (top and seat angle, and stiffened welded-seat connections). Since Chisala's model is expressed in a general form, equivalent analytical models for both types of connections were created and using a matrix structural analysis program written in MATLAB, those models were analyzed and the results were utilized to determine the necessary parameters of Chisala's model. Using two series of linear regression

analysis for each type of connection, a power relation describing the plastic stiffness (K_p) as a function of the initial stiffness (K_i), and another power relation describing the intercept-constant (M_0) as a function of geometric dimensions of the connection components, were derived from the general form of Chisala's model. These two functions were used to plot the analytical moment-rotation curves for the two mentioned types of connections. As a means of verification, 34 top and seat angle (TSA), and 33 stiffened welded-seat (SWS) numerical connection models were created using Abaqus software. These numerical models were then analyzed utilizing FEA, and the moment-rotation curve for each model was plotted. The analytical and numerical models were compared at last, and the following conclusions were made:

1- Chisala's model can precisely predict the moment-rotation curve for top and seat angle (TSA) and stiffened welded-seat (SWS) connections.

2- Using Chisala's model to determine the moment-rotation curve is very efficient since it has fewer parameters (there are some other models which have fewer parameters but Chisala's model seems to have the least possible count of parameters before compromising its precision), and these parameters are independent and easy to determine.

3- Since Chisala's model is expressed in a general form, creating the equivalent analytical model for any type of steel connection, is the key step in using Chisala's model to its full potential. The equivalent analytical model can be created using a system of linear springs, each resembling the stiffness of connection components.

4- The precision of Chisala's model in predicting the moment-rotation curve for top and seat angle, and stiffened welded-seat connections is acceptable, therefore further research on determining the moment-rotation curve for other types of steel connection using this model, is encouraged.

5- Geometric dimensions of connection components, do affect their flexural performance and it appears that geometric dimensions of the top angle control the performance for both types of connections.

6- The nonlinear performance of these connections begins at the top angle and extends to other components of the connection.

7- The stiffened welded-seat (SWS) connection appears to be stiffer than the top and seat angle (TSA) connection, and both connections exhibit a semi-rigid performance.

References

[1] R.M. Richard, W.-k. Hsia, M. Chmielowiec, Derived moment rotation curves for double framing angles, Computers & Structures 30(3) (1988) 485-494.

[2] C.W. Lewitt, W.H. Munse, E. Chesson, Restraint characteristics of flexible riveted and bolted beam-to-column connections, University of Illinois. Engineering Experiment Station. Bulletin ; No. 500, 1969.

[3] M.J. Frye, G.A. Morris, Analysis of flexibly connected steel frames, Canadian Journal of Civil Engineering 2(3) (1975) 280-291.

[4] R.M. Richard, B.J. Abbott, Versatile elastic-plastic stress-strain formula, Journal of the Engineering Mechanics Division 101(4) (1975) 511-515.

[5] K.M. Ang, G.A. Morris, Analysis of three-dimensional frames with flexible beam–column connections, Canadian Journal of Civil Engineering 11(2) (1984) 245-254.

[6] E. Attiogbe, G. Morris, Moment-rotation functions for steel connections, Journal of Structural Engineering 117(6) (1991) 1703-1718.

[7] N. Kishi, M. Komuro, W.F. Chen, Four-parameter power model for M-θ curves of end-plate connections, Proceedings of connection in steel structures V. Amsterdam (2004) 99-110.

[8] A. Abolmaali, J.H. Matthys, M. Farooqi, Y. Choi, Development of moment–rotation model equations for flush end-plate connections, Journal of Constructional Steel Research 61(12) (2005) 1595-1612.

[9] V.L. Tran, Moment-rotation-temperature model of semi-rigid cruciform flush endplate connection in fire, Fire Safety Journal 114 (2020) 102992.

[10] S.S. Lee, T.S. Moon, Moment–rotation model of semi-rigid connections with angles, Engineering Structures 24(2) (2002) 227-237.

[11] A. Azizinamini, Cyclic characteristics of bolted semi-rigid steel beam to column connections, College of Engineering, University of South Carolina, Columbia, SC, USA, 1985.

[12] L. Calado, G. De Matteis, R. Landolfo, Experimental response of top and seat angle semi-rigid steel frame connections, Materials and Structures 33(8) (2000) 499-510.

[13] Z. Kong, S.-E. Kim, Moment-rotation behavior of top-and seat-angle connections with double web angles, Journal of Constructional Steel Research 128 (2017) 428-439.

[14] A. Azizinamini, J.B. Radziminski, Static and Cyclic Performance of Semirigid Steel Beam to Column Connections, Journal of Structural Engineering 115(12) (1989) 2979-2999.

[15] M.L. Chisala, Modelling M–φ curves for standard beam-to-column connections, Engineering Structures 21(12) (1999) 1066-1075.

[16] F.H.S. Gilio, L.C.M. Vieira, M. Malite, Stability and moment-rotation behavior of cold-formed steel purlins with sleeved bolted connection, Engineering Structures 171 (2018) 658-672.

[17] G. Zhou, Y. An, Z. Wu, D. Li, J. Ou, Analytical model for initial rotational stiffness of steel beam to concrete-filled steel tube column connections with bidirectional bolts, Journal of Structural Engineering 144(11) (2018) 04018199.

[18] B. Zhao, C. Sun, H. Li, Study on the moment-rotation behavior of eccentric rectangular hollow section cross-type

connections under out-of-plane bending moment and chord stress, Engineering Structures 207 (2020) 110211.

[19] M. Mofid, M.R.S. Mohammadi, S.L. McCabe, Analytical approach on endplate connection: ultimate and yielding moment, Journal of Structural Engineering 131(3) (2005) 449-456.

[20] M.S. Ghobadi, A. Mazroi, M. Ghassemieh, Cyclic response characteristics of retrofitted moment resisting connections, Journal of Constructional Steel Research 65(3) (2009) 586-598.

[21] Recommended Seismic Design Criteria for New Steel Moment-frame Buildings: FEMA 350, Federal Emergency Management Agency, 2000.

[22] E.C.f. Standardization, Eurocode 3, Design of steel structures - Part 1-8: Design of joints, Brussels, 2003.